Journal of Thermal Analysis and Calorimetry (2024) 149:4195–4207
https://doi.org/10.1007/s10973-024-12977-0

Mixed convection of nano-encapsulated phase change suspensions in a wavy wall lid-driven trapezoid cavity

Mehdi Ghalambaz[1] · Kasra Ayoubi Ayoubloo[2] · Masoud Mozaffari[3] · Talal Yusaf[4,1] · Mohammad S. Islam[5] · Nehad Ali Shah[6] · Manuel Baro[7]

Received: 23 July 2023 / Accepted: 31 January 2024 / Published online: 15 April 2024

Abstract
The improvement of heat transfer and energy storage are crucial tasks in many renewable energy applications. The thermal and hydrodynamic performances of a nano-encapsulated phase change material (NEPCM) suspension are investigated under a mixed convective heat transfer regime inside a trapezoidal enclosure. As the host fluid and dispersed NEPCM particles circulate in the enclosure, the nanoparticle cores absorb/release heat and undergo a phase transition process, enhancing heat transfer. The governing equations were scaled into a general non-dimensional format and then solved by the finite element method. The influence of nanoparticles fusion temperature and concentration, as well as the wavy wall characteristics and Richardson number, was addressed on heat transfer. A suitable fusion temperature of the nanoparticles can boost the heat transfer rate by 8%. Furthermore, by employing 5% NEPCM particles at a dimensionless fusion temperature of 0.1, the Nusselt number achieved was 9.05. This marks a significant 37% rise when contrasted with a base fluid, which only had a Nusselt number of 5.7.

Keywords Wavy wall lid-driven enclosure · Nano-encapsulated phase change material suspension · Mixed convection · Heat transfer enhancement

Introduction

The use of nano-encapsulated phase change materials (NEPCMs) has found important applications in heat transfer systems. NEPCMs are nano-sized capsules containing phase change materials (PCMs) that absorb, store, and release heat during phase transitions [1, 2]. This unique property makes them ideal for enhancing the thermal performance of various systems, including electronic devices [3], solar thermal systems [4], and foods [5].

In the context of heat transfer, mixed convection plays a crucial role in determining the efficiency of a system. Mixed

✉ Mehdi Ghalambaz
mehdighalambaz@duytan.edu.vn;
ghalambaz.mehdi@gmail.com

Kasra Ayoubi Ayoubloo
kasra.ayoubi@yahoo.com

Masoud Mozaffari
masoodmozafari66@yahoo.com

Talal Yusaf
t.yusaf@cqu.edu.au

Mohammad S. Islam
mohammadsaidul.islam@uts.edu.au

Nehad Ali Shah
nehadali199@yahoo.com

Manuel Baro
mbaro@itsncg.edu.mx

[1] College of Engineering, Almaaqal University, Basra 61003, Iraq

[2] Department of Mechanical Engineering, Shahid Chamran University of Ahvaz, Ahvaz, Iran

[3] Department of Mechanical Engineering, Najafabad Branch, Islamic Azad University, Najafabad 85141-43131, Iran

[4] School of Engineering and Technologies, Central Queensland University, Rockhampton, QLD 4701, Australia

[5] School of Mechanical and Mechatronic Engineering, University of Technology Sydney, Ultimo, NSW 2007, Australia

[6] Department of Mathematics, Saveetha School of Engineering, Chennai, Tamilnadu 602105, India

[7] Researcher at the Tecnológico Nacional de México Campus Nuevo Casas Grandes, Nuevo Casas Grandes, Chih., México

convection, a combination of natural and forced convection, is a complex phenomenon that occurs when the buoyancy forces and shear-induced forces are of comparable magnitude. The study of mixed convection of NEPCM suspensions, therefore, becomes essential in optimizing the thermal performance of systems employing these materials [6, 7].

The geometry of the system also significantly influences the heat transfer characteristics. In this regard, the trapezoid cavity, due to its non-uniform cross section, presents an interesting case for the study of mixed convection [8, 9]. The wavy wall of the trapezoid cavity further adds to the complexity of the flow and heat transfer phenomena [10]. The lid-driven flow in such a cavity, induced by the motion of one of the walls, is a common feature in many engineering applications, including lubrication technologies, cooling of electronic equipment, and process engineering.

The present research aims to investigate the complex interplay between the mixed convection phenomena, the unique properties of NEPCM suspensions, and the intricate geometry of a wavy wall lid-driven trapezoid cavity. The literature review related to these aspects is briefly explored here.

The literature on mixed convection in lid-driven cavities is extensive. Early studies focused primarily on the case of a square cavity with smooth walls. For instance, the works of Shankar and Deshpande [11] and Ece and Buyuk [12] provided valuable insights into the flow patterns and heat transfer characteristics in such systems. However, the focus has gradually shifted toward more complex geometries and boundary conditions, reflecting the practical scenarios encountered in engineering applications. Recently, several configurations of the mixed convection heat transfer have been monitored to gain a better understanding of the thermal and hydrodynamic performances, such as mixed convection in lid-driven cavities in the presence of rotating cylinder [13], double-pipe heat exchanger [14], internal heat generation [15], partial porous media [16], cylindrical [17], and square cylinders [16]. The wavy wall enclosures have also received considerable attention [18].

Very recently, the free convection of NEPCMs in enclosures has received notable attention. Simple geometries, such as rectangles [19], and also complex geometries, such as T-shape [20], grooved wall [21], infinite-shaped [22], and crescent [23], have been investigated. However, the study of mixed convection of NEPCM suspensions in complex geometries has remained relatively unexplored. A few studies, such as those by Herouz et al. [24] and Qasem et al. [10], have evaluated the mixed convective heat transfer of NEPCMs inside hexagonal [24] and trapezoidal [10] lid-driven cavities. The mixed convection of NEPCM suspensions in the presence of rotating cylinders [25, 26] is another aspect

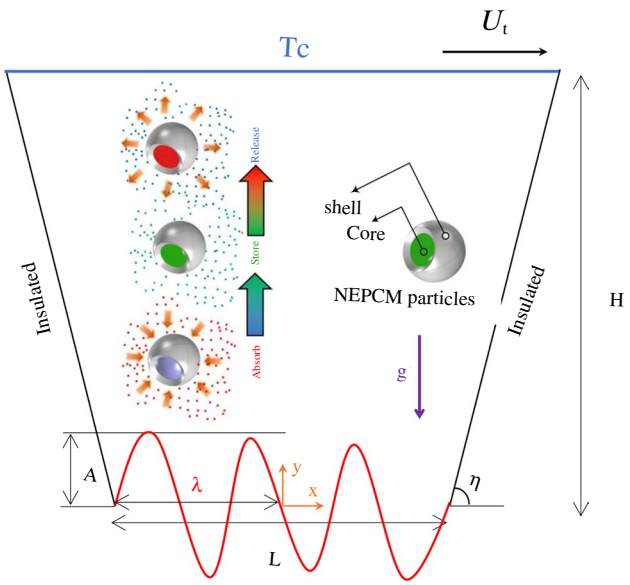

Fig. 1 A schematic representation of the wavy wall trapezoidal cavity's model and computational domain

of mixed convection flows, and its mixed convection flow nature is completely different from lid-driven cavities.

Despite the intricate nature of convective heat transfer in NEPCM suspensions within mixed convection flows, there is a noticeable lack of comprehensive studies in the literature addressing this specific topic. Most of the available literature has investigated the natural convection heat transfer of NEPCM suspensions. However, mixed convection induces completely different convection heat transfer characteristics due to the involved forced convection features of the fluid flow. Thus, the present study aims to address the mixed convection heat transfer of NEPCM suspensions in a wavy wall lid-driven trapezoidal cavity.

Physical model

Model description

Figure 1 presents a diagrammatic representation of a long, two-dimensional trapezoidal enclosure with a wavy base. This enclosure is filled with a blend of water and NEPCM. The model is two-dimensional due to the extended length of the enclosure. The nanoparticles within the mixture take up a specific volume ratio, symbolized as ϕ, which fills the cavity. The top cold-driven lid of the enclosure, denoted as T_c, moves at a velocity, U_t, to the right. Conversely, the bottom wall maintains a high temperature, symbolized as Th. The enclosure's bottom length L, and height H are equal, such that $L = H$.

The nanoparticles, depicted in an enlarged view in Fig. 1, are encapsulated in a PCM. The PCM core transitions between liquid and solid states, enabling the absorption or release of latent heat at a fusion temperature T_f, where T_f adopts magnitudes between T_c and Th. Figure 1 also illustrates the various stages of a nanoparticle's phase change cycle, including states like a liquid hotcore, a solid coldcore, and a regular state.

The wavy bottom wall is controlled by a parameter, wavenumber (λ), and wave amplitude A, while η symbolizes the angle of the trapezoidal shape, as shown in Fig. 1. Each nanoparticle is composed of a nonadecane core (PCM) and polyurethane (PU) shell. This type of NEPCM suspension was adopted as it was synthesized and examined in [27]. The NEPCM mixture is uniform, with minimal slippage between the base fluid and the nanoparticles inside.

Considering the minuscule size of these encapsulated particles, there is no significant temperature difference within the particles, making them apt for the lamp model of nanoparticles and phase change within particle cores. The primary properties of the host fluid, the PCM core, and the shell are listed in Table 1. Notably, the core's fusion latent heat and temperature are 211 kJ kg^{-1} and 32 °C, respectively, as examined by Barlak et al. [27].

The wavy wall is defined by the equation:

$$y = A \times \sin(2\pi(x/\lambda)) \tag{1}$$

In this equation, λ signifies the wavelength, and A represents the amplitude of the wave.

Governing equations

The governing equations for heat transfer of NEPCM in the enclosure are the conservation of mass, momentum, and energy, which can be expressed as [28, 29]:

$$\nabla \mathbf{u} = 0 \tag{2}$$

$$\rho_b(\mathbf{u}.\nabla)\mathrm{u} = -\nabla p + \mu_b \nabla^2 \mathbf{u} + \rho_b \beta_b \mathrm{g}\left(T - T_c\right) \tag{3}$$

$$\left(\rho C_p\right)_b \mathbf{U}.\nabla T = k_b \nabla^2 T \tag{4}$$

where the bold symbols show the vector field. Here, $\boldsymbol{u}$ is the velocity field (including x-velocity u and y-velocity v), and T is the scaler temperature field. The gravity field is denoted by $\boldsymbol{g}$. The properties of thermal conductivity (k), density (ρ), dynamic viscosity (μ), and volume expansion (β) are used in the equations. The subscript b indicated the NEPCM suspension. The no-slip and no-permeability were applied on all surfaces. The lid velocity is considered as $u = U_t$. For the sidewalls $\partial T/\partial n = 0$ where n is the surface normal. For the top wall $T = T_c$ and for the bottom wall $T = T_c$. A reference pressure point $p = 0$ was also considered at the bottom left corner.

More details about the heat capacity of NEPCM particles and other bulk properties can be found in [28]. The densities of NEPCM suspension and NEPCM particles are computed as [30]:

$$\rho_b = (1 - \phi)\rho_f + \phi\rho_p \tag{5}$$

$$\rho_p = (1 + \iota)\left(\rho_{co}\rho_{sh}\right)\left(\rho_{sh} + \iota\rho_{co}\right)^{-1} \tag{6}$$

where subscript f and sh denote the base fluid and NEPCM shell. Here, ι and φ are the core–shell mass ratio ($\iota \sim 0.447$[27]), and NEPCM concentration, respectively. The heat capacities of the suspension (Cp_b) and NEPCM particle with no phase change (Cp_p) are evaluated as [30–32]:

$$Cp_b = \frac{\rho_f Cp_f(1 - \phi) + \rho_p Cp_p \phi}{\rho_b} \tag{7}$$

$$Cp_p = \frac{\left(Cp_{co} + \iota Cp_{sh}\right)\left(\rho_{co}\rho_{sh}\right)}{\left(\rho_{sh} + \iota\rho_{co}\right)\rho_p} \tag{8}$$

The total specific heat capacity of the nanoparticle core, including sensible and latent heat, is evaluated as [30, 33]:

$$Cp_c = Cp_{co,l} + \frac{\pi}{2}\left(\frac{h_{sf}}{\delta T} - Cp_{co,l}\right)\sin\left(\pi\frac{T - T_f + \delta T/2}{\delta T}\right) \times \begin{cases} 0 & T < T_f - \delta T/2 \\ 1 & T_f - \delta T/2 < T < T_f + \delta T/2 \\ 0 & T > T_f + \delta T/2 \end{cases} \tag{9}$$

Table 1 Thermophysical properties of the shell (PU) and core (Nonadecane) of NEPCM particles as well as the host fluid [27]

	ρ/kg m^{-3}	μ/kg m^{-1}s^{-1}	C$_p$ /kJ kg^{-1}K^{-1}	k/W m^{-1}K^{-1}	β/K^{-1}
Nonadecane*	721	–	2037	–	–
Host fluid	997.1	8.9×10^{-4}	4179	0.613	21×10^{-5}
PU	786	–	1317.7	–	17.28×10^{-5}

*The latent heat fusion for NEPCM cores is 211 kJ.kg^{-1}, and their phase change temperature stands at 32 °C [27]

where the subscripts p, co, and l represent the NEPCM particle, NEPCM core, and core in liquid form, respectively. The symbol h_{sf} is the latent heat of phase change, T_f denotes the fusion temperature, and δT is the phase change interval. By substituting Eq. (9) in Eq. (8), the effective specific heat capacity of the NEPCM particle can be obtained. The suspension's effective thermal expansion, effective thermal conductivity, and effective dynamic viscosity are computed using [33–35]:

$$\beta_b = (1-\phi)\beta_f + \phi\beta_p \tag{10}$$

$$\frac{k_b}{k_f} = 1 + \mathrm{Nc}\phi \tag{11}$$

$$\frac{\mu_b}{\mu_f} = 1 + \mathrm{Nv}\phi \tag{12}$$

where Nc and Nv can be obtained by curve fitting on experimental data. For more details, see [28].

Scaling the governing equations

To reveal the inherent characteristics of the NEPCM suspension, the governing equations and their associated boundary conditions undergo a remarkable transformation, transitioning into a realm characterized by dimensionless quantities. As a result, a collection of non-dimensional variables gracefully enters the spotlight, choreographing a magnificent and captivating metamorphosis.

$$(X,Y,N,a,\lambda) = \frac{(x,y,N,a,\lambda)}{H}, \mathbf{U} = \frac{\mathbf{u}}{U_t}, P = \frac{p}{\rho U_t^2}, \theta = \frac{T-T_c}{Th-T_c} \tag{13}$$

By invoking the scaled parameters, the governing equations are reduced to a scaled format:

$$\nabla \mathrm{U} = 0 \tag{14}$$

$$\left(\frac{\rho_b}{\rho_f}\right)(\mathbf{U}.\nabla)\mathbf{U} = -\nabla P + \frac{(1+N\nu\varphi)}{\mathrm{Re}}\nabla^2\mathbf{U} + \frac{(\rho\beta)_b}{(\rho\beta)_f}Ri\theta \tag{15}$$

$$\left((1-\varphi)+\varphi\lambda+\varphi\frac{f}{\delta \mathrm{Ste}}\right)\mathbf{U}.\nabla\theta = \frac{1}{\mathrm{Pr}\,\mathrm{Re}}(1+Nc\varphi)\nabla^2\theta \tag{16}$$

where the term $(1-\varphi)+\varphi\lambda+\varphi\frac{f}{\delta \mathrm{Ste}}$ can be considered as heat capacity ratio (Cr). Richardson (Ri), Reynolds (Re), Prandtl (Pr), Grashof (Gr), and Stefan numbers are introduced based on host fluid as:

$$\begin{gathered}\mathrm{Gr} = \frac{\rho_f^2 g\beta_f \Delta T H^3}{\mu_f^2},\ \mathrm{Pr} = \frac{\mu_f}{\rho_f\alpha_f},\ \mathrm{Re} = \frac{\rho_f U_t H}{\mu_f},\\ \mathrm{Ri} = \frac{\mathrm{Gr}}{\mathrm{Re}^2},\ \mathrm{Ste} = \frac{(\rho C_p)_f \Delta T(\rho_{sh}+\iota\rho_{co})}{h_{sf}\rho_{co}\rho_{sh}}\end{gathered} \tag{17}$$

The remaining dimensionless parameters are the heat capacity ratio (λ) and scaled phase transient interval (δ):

$$\begin{gathered}\lambda = \frac{(C_{p,co}+\iota C_{p,sh})\rho_{co}\rho_{sh}}{(\rho C_p)_f(\rho_{sh}+\iota\rho_{co})},\ \delta = \frac{\delta T}{Th-T_c},\\ \left(\frac{\beta_b}{\beta_f}\right) = (1-\phi)+\phi\frac{\beta_p}{\beta_f},\quad \left(\frac{\rho_b}{\rho_f}\right) = (1-\phi)+\phi\frac{\rho_p}{\rho_f}\end{gathered} \tag{18}$$

Besides, it was assumed that the NEPCM expansion is close to the host fluid and using data in Table 1; hence, $(\beta_b/\beta_f) \sim 1$ and $(\rho_p/\rho_f) \sim 0.74$. Ultimately, f is obtained in a transformed as:

$$f = \frac{\pi}{2}\sin\left(\frac{\pi}{\delta}(\theta-\theta_f+\delta/2)\right)\begin{cases}0 & \theta < \theta_f-\delta/2\\ 1 & \theta_f-\frac{\delta}{2} < \theta < \theta_f+\delta/2\\ 0 & \theta > \theta_f+\delta/2\end{cases} \tag{19}$$

and $\theta_f = \frac{T_f-T_c}{Th-T_c}$. The bottom wavy shape is transformed into the following scaled format:

$$\mathrm{Y} = a \times \sin(2\pi(\mathrm{X}/\omega)) \tag{20}$$

Ultimately, the zero velocity and permeability ($\boldsymbol{U}=0$) were applied to all surfaces, and the lid velocity was scaled as non-dimensional x velocity = 1. The insulated walls were explained as $\partial\theta/\partial N = 0$, and the top and bottom surfaces are thermally defined as $\theta = 0$, and $\theta = 1$, respectively.

Characteristics parameters

The local Nusselt number, $\mathrm{Nu_l} = hH/k_f$ is obtained as:

$$\mathrm{Nu_l} = -(1+\mathrm{Nc}\varphi)\left(\frac{\partial\theta}{\partial N}\right)\Big|_{\text{Wavy wall}} \tag{21}$$

in which, h is the coefficient of the convective heat transfer. The average Nusselt (Nu) is obtained by integration as:

$$\mathrm{Nu} = \frac{1}{L}\int_0^L Nu_l \mathrm{d}L \tag{22}$$

where L is the scaled characteristics length along the wall. Ultimately, the scaled stream function (ξ) is computed as:

$$\nabla^2\xi = -\nabla \times \mathbf{U} \tag{23}$$

where $-\nabla \times \mathbf{U}$ represents the curl of the flow velocity vector. Besides, $\xi = 0$ was applied on all surfaces as the boundary condition [36, 37].

Numerical method and model verification

Finite element numerical method

The FEM was utilized to decipher the fundamental equations along with their initial conditions and boundary parameters. This approach was successful in managing nonlinear sink/source parameters that arose from phase transition (refer to [38, 39]). By using a weak form of the primary equations and a second-order approximation for heat and momentum equations, the Gauss quadrature integration was used at an elemental level to create a set of algebraic residual equations. The Newton method [38, 39] was employed to solve these equations iteratively and interdependently, incorporating a damping coefficient of 0.8 to enhance convergence. In conjunction with the Newton method, the PARDISO parallel solver was used to enable parallel computations across multiple processing units (refer to [40, 41]). A relative solution precision of $O(10^{-4})$ was used for computations.

Mesh study

The impact of grid size on accuracy of the results was evaluated by simulating the mixed convection heat transfer of NEPCM suspension for a test scenario with Ste = 0.3, $\omega = 1/2$, $\varphi = 0.05$, Re = 100, Ri = 1.0, $\delta = 0.05$, $\lambda = 0.33$, $a = 0.15$, $\theta_f = 0.2$, $Nv = 12.5$, $\eta = 60°$, Pr = 6.2, and Nc = 23.8. A structured mesh divided the solution domain, with the size of the mesh defined by the mesh resolution parameter, Nm. The details of the created structures and the computed average Nusselt number are showcased in Table 2. The local Nusselt number is also plotted in Fig. 3 along the hot wall (Fig. 2).

Table 2 Specifications of Mesh and Nu for four examined mesh sizes

Cases	Triangles	*Nu*	*%difference
I	5990	8.0848	0.82
II	10,041	8.1266	0.31
III	20,924	8.1589	0.09
IV	31,722	8.151	0.012
V	52,340	8.152	–

*%difference = $(Nu\text{-}Nu_{@Case\ V}) \times 100/Nu_{@Case\ V}$

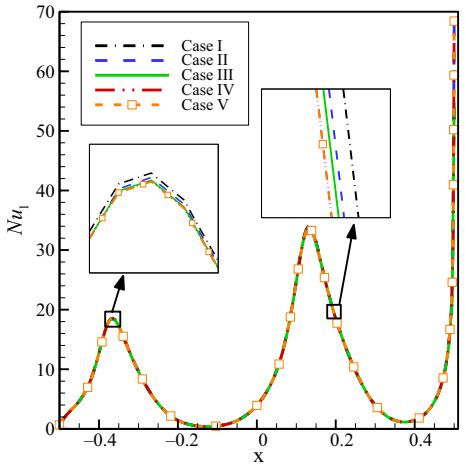

Fig. 2 Local Nusselt number at the wavy wall for the adopted mesh resolutions

A structured grid partitioned the model's domain, with the grid size determined by the grid resolution parameter. Table 2 presents the specifics of the generated structures and the calculated average Nusselt number. The local Nusselt number is also graphically represented in Fig. 3 along the hot wavy surface.

Table 2 demonstrates a consistent and noticeable increase in computational requirements as the mesh resolution escalates. This trend is expected as the quantity of mesh elements and edge elements grows in tandem with the mesh resolution. The mesh Case III yields an error of only 0.09% compared to a very fine mesh Case V, which is satisfactory for the graphical representation of the results and most practical applications. Consequently, the mesh case III was selected for the remaining simulations. Figure 3 provides a visualization of the chosen mesh.

Model validation

In order to assess the reliability of the employed code, this study compares its results with two previously published works. Firstly, Nu from the current research is checked against the findings of [42], who investigated the free convection of Cu-water inside an annulus. Table 3 lists *Nu* of the current research and the ones presented in [42] for various concentrations of Cu nanoparticles, which indicates close outcomes. As another check, the isotherms of current research are compared to the findings of [43] for free convection in a square enclosure with a temperature difference between vertical surfaces and zero flux top and bottom. Figure 4 shows a close alignment between the two studies. Table 4 provides Nu values from different references for mixed connective heat transfer within a lid-driven square cavity equipped with a top hot-driven lid, cool lower surface,

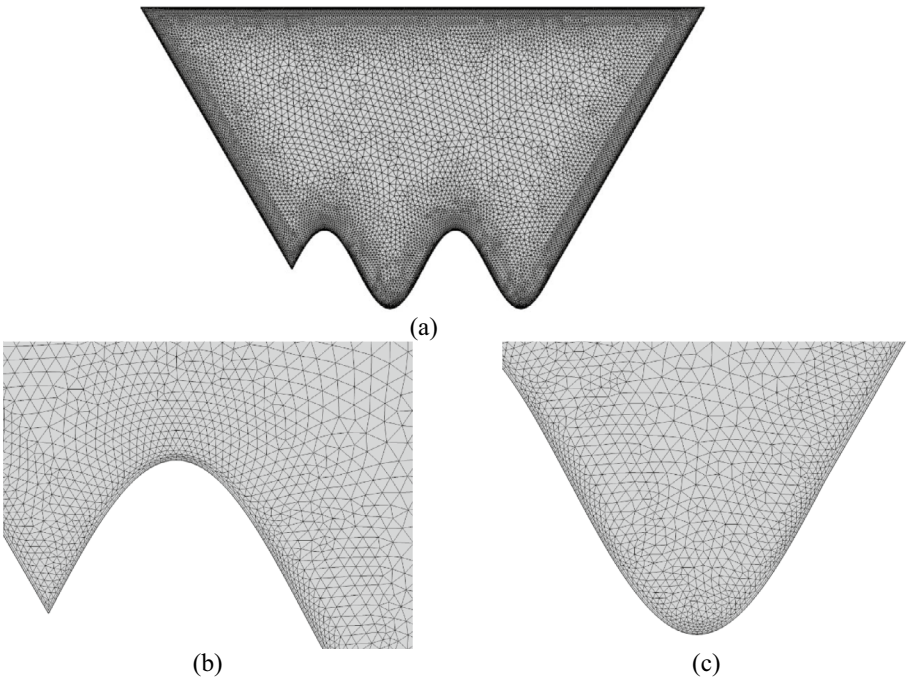

Fig. 3 The adopted mesh with Case III: **a** a full overview of the mesh, **b** magnified view at a wavy peak, **c** magnified view at the lowest point of the wavy pattern

and zero heat flux side walls. Ultimately, Fig. 5 compares the streamlines and temperature distributions between the current simulations and those of [37, 44]. The top surface was hot lid-driven, the bottom was cold, and the side surfaces were at zero heat flux. Table 4 and Fig. 5 also confirm good alignments between the two studies.

Table 3 Nusselt of current research and those of [42]

Study	$\varphi=0.01$	$\varphi=0.02$	$\varphi=0.03$
Matin and Pop [42]	5.66	5.89	6.02
Current research	5.62	5.88	6.07

Table 4 *Nu* for a top lid-driven square cavity with a hot top surface, a cool lower surface, and zero heat flux at side surfaces when Gr = 100 and Pr = 0.71

Ri	Re	Waheed [45]	Roy et al. [37]	Iwatsu et al. [46]	Present study
100	1	1.00033	0.998	–	1.000
0.01	100	2.03116	1.967	1.94	2.034
6.25×10^{-4}	400	4.02462	4.004	3.84	4.036
4×10^{-4}	500	4.52671	4.509	–	4.527
1×10^{-4}	1000	6.48423	6.443	6.33	6.377

Results and discussion

Here, the influence of NEPCMs fraction ($0<\varphi<0.05$), wavelength ($1/4<\omega<1$), wave amplitude ($0<a<0.2$), nanoparticles' fusion temperature ($0.1<\theta_f<0.9$), and Richardson number $0.001<\mathrm{Ri}<0.1$ on the Nu was addressed. The following configuration is considered as

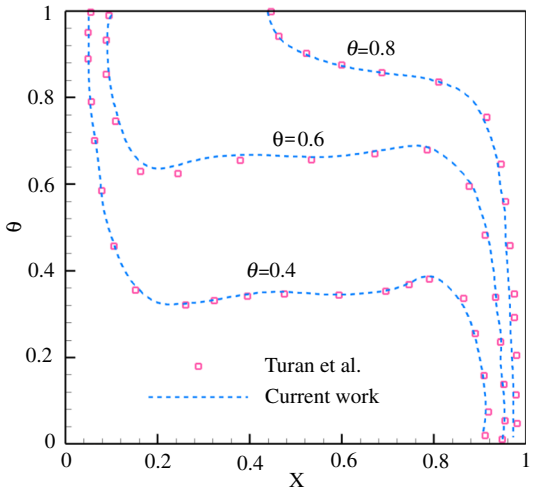

Fig. 4 A comparison between the simulated isotherm distributions obtained in the current study and the ones in [43]

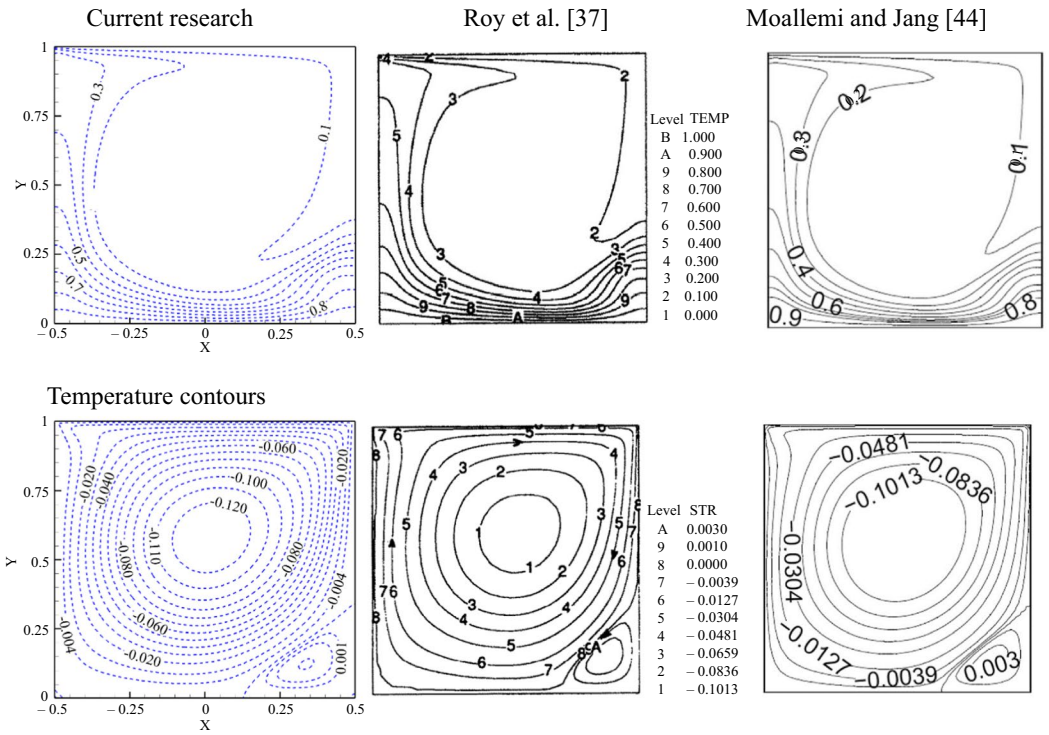

Fig. 5 Illustration of the contrast between temperature distribution and fluid flow patterns inside a lid-driven cavity. The setup includes a top cool surface, a bottom hot surface, and zero heat flux at the sides. The specific conditions for this comparison are Reynolds number of 500, Prandtl number of 1.0, and Richardson number of 0.4. The current research versus Roy et al. [37] and Moallemi and Jang [44]

a basis for the non-dimensional parameters Re = 100, Ri = 0.1, $\theta_f = 0.2$, Pr = 6.2, Ste = 0.3, $\lambda = 0.33$, $\delta = 0.05$, Nc = 23.8, Nv = 12.5, $\eta = 60°$, $\varphi = 0.05$, $a = 0.1$. Otherwise the value of the parameter will be reported.

Figure 6 serves to illuminate the impact of two key parameters—wave amplitude (a) and wavelength (ω)—associated with the wavy wall on Nu. A grow of wavelength and wave amplitude both contribute positively to the augmentation of the Nusselt number. This suggests that these parameters are vital in enhancing heat transfer efficiency.

Subsequently, Fig. 7 provides a detailed examination of the local Nusselt number in correlation with several wave amplitudes. This deepens the understanding of how the precise heat transfer at a specific location on the wavy wall changes with wave amplitude.

Further elucidation on this topic is provided by Fig. 8, which offers an inclusive perspective of the temperature distribution, streamlines, and phase transient patterns (Cr). When studying the fluctuations of Nu_1 for the assessed values of wave amplitude (a), it becomes evident that an increase in the wave amplitude corresponds with a sharp surge in Nu_1 at each wave's peak. However, this sharply declines within each wave's trough, pointing toward an interesting alternating pattern of heat transfer across the wavy surface.

A closer inspection of the isotherms in Fig. 8 reveals a distinct thermal behavior. While the troughs display a consistent hot region with an almost non-existent temperature gradient, a substantial temperature gradient becomes apparent at each peak. This indicates the intriguing thermal dynamics at play due to the undulating nature of the wall. The undulations seem to create pockets of trapped fluid in the troughs, while the peaks exhibit a high degree of surface exposure to the fluid flow stimulated by mixed convection.

Complementing this, the streamlines demonstrate that the flow circulation predominantly transits over the peaks and is less inclined to penetrate into the troughs. The interaction of these high and low variations, as outlined in Fig. 6, contributes to the overall enhancement of the heat transfer rate, represented by Nu.

However, the phase transient pattern (Cr) was minimally affected by changes in wave amplitude, as depicted in Fig. 8. The region where phase transitions occur appears to be substantially distanced from the wavy surface. This implies that the wave amplitude has a negligible influence on phase change dynamics, which occur at a sufficient distance from the undulating surface.

Figure 9 shows the influence of Richardson number and fusion temperature on Nu. An increase in Richardson number increases Nu, while a rise in fusion temperature reduces Nu. For a fixed Reynolds number, an increase of Ri can be interpreted as a stronger Rayleigh number. A rise IN Rayleigh number leads to better natural convection

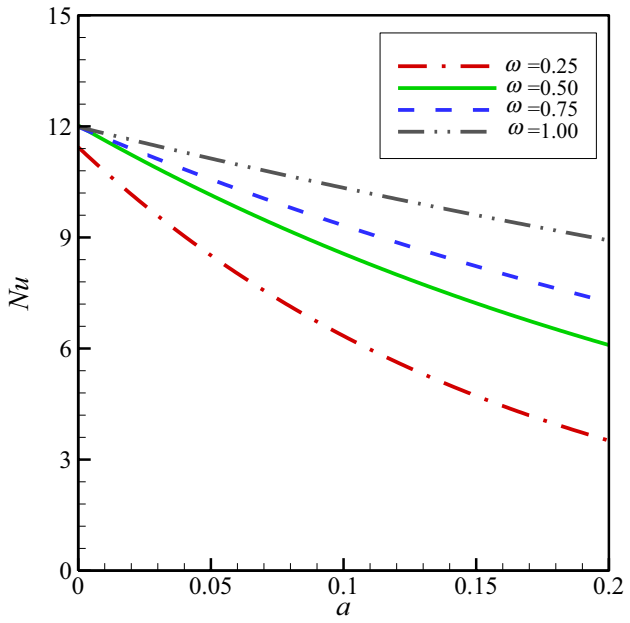

Fig. 6 Effect of wave amplitude (a) and wave length (ω) on the Nu

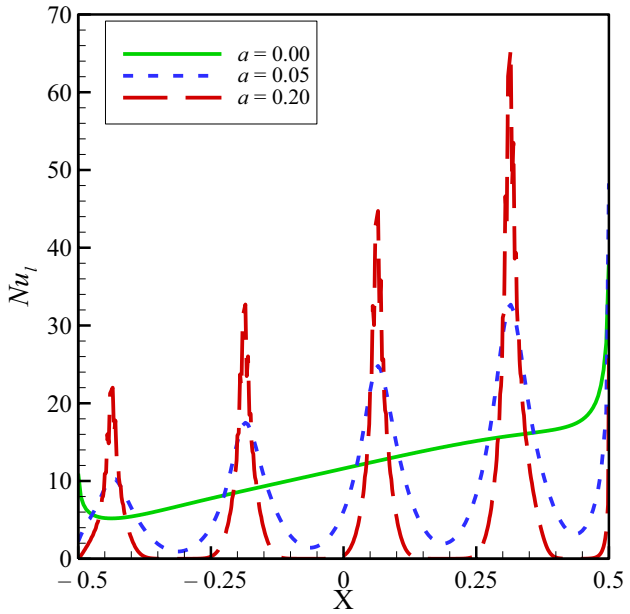

Fig. 7 Local Nusselt number for various wave amplitudes (a)

circulation. The natural convection circulation tends to induce upward convection flows over troughs and further improve the temperature gradients along the wavy wall, particularly at peaks. This observation can be confirmed by Nu_l in Fig. 10. An increase of Ri promotes Nu_l sharply at peaks, but it has minimal impact on the Nu_l inside troughs. Attention to the temperature distributions for various Ri numbers (see Figs. 11 and 12) also shows a better temperature gradient inside troughs. Thus, an increase IN Richardson number improved the Nu_l and, consequently, Nu.

Moreover, increased Ri slightly shifts the phase transient region upward due to the increasing strength of natural convection circulations. A rise in θ_f moves the phase transient region from the bottom next to the wavy wall ($\theta_f=0.9$) toward the middle ($\theta_f=0.5$) and the top wall ($\theta_f=0.1$), as depicted in Fig. 11. The phase transient region shapes around isotherms with a temperature to the fusion temperature of NEPCM cores. Since the isotherms next to the hot wall have a temperature close to the hot wall, the phase transient for $\theta_f=0.9$ has occurred just next to the wavy wall. Moreover, the variation of fusion temperature imposes minimal effects on the overall temperature distributions and streamlines. This is since the phase change of the NEPCM particles core imposes local impacts on the flow and temperature, but the moving lid and the imposed thermal boundary conditions dictate the overall temperature distribution and flow circulation. Figure 9 depicts that a small fusion temperature ($\theta_f=0.1$) can provide a much better heat transfer rate than a large one. This can be attributed to the shape of the transient region, which is quite extended for the case of $\theta_f=0.1$ compared to the case of $\theta_f=0.9$, which is compacted next to the hot wavy wall. A variation of fusion temperature from $\theta_f=0.9$ to $\theta_f=0.1$ raises Nu from 6.3 to 6.85, which is about 8% enhancement. Such enhancement can be achieved by seldom adjusting the fusion temperature of NEPCM particles.

Figure 13 offers a comprehensive exploration of how the fraction of particles and their fusion temperature affect the average Nusselt number (Nu). It is observed that an increase in the particle fraction leads to an elevation in the Nusselt number. This relationship suggests that higher particle fractions have a direct and beneficial impact on heat transfer efficiency.

The rise in particle fraction delivers dual benefits to the heat transfer process. Firstly, it brings thermal conductivity enhancement to the suspension, an essential factor in effective heat transmission. Secondly, it augments the heat transfer rate by increasing the heat capacity ratio. This increase stems from the heat capacity due to the contribution of latent heat, a crucial element in the thermodynamics of phase change materials.

Interestingly, the peak Nusselt number can be achieved when the fusion temperature aligns closely with the temperature of the cold lid-driven wall situated at the top. This finding corroborates the outcomes demonstrated in Fig. 9, lending additional credibility to the observed results.

To exemplify this, consider the use of nano-encapsulated phase change material (NEPCM) particles at a concentration of 5%, with a fusion temperature $\theta_f=0.1$. This configuration results in a Nusselt number of 9.05. In contrast, with a

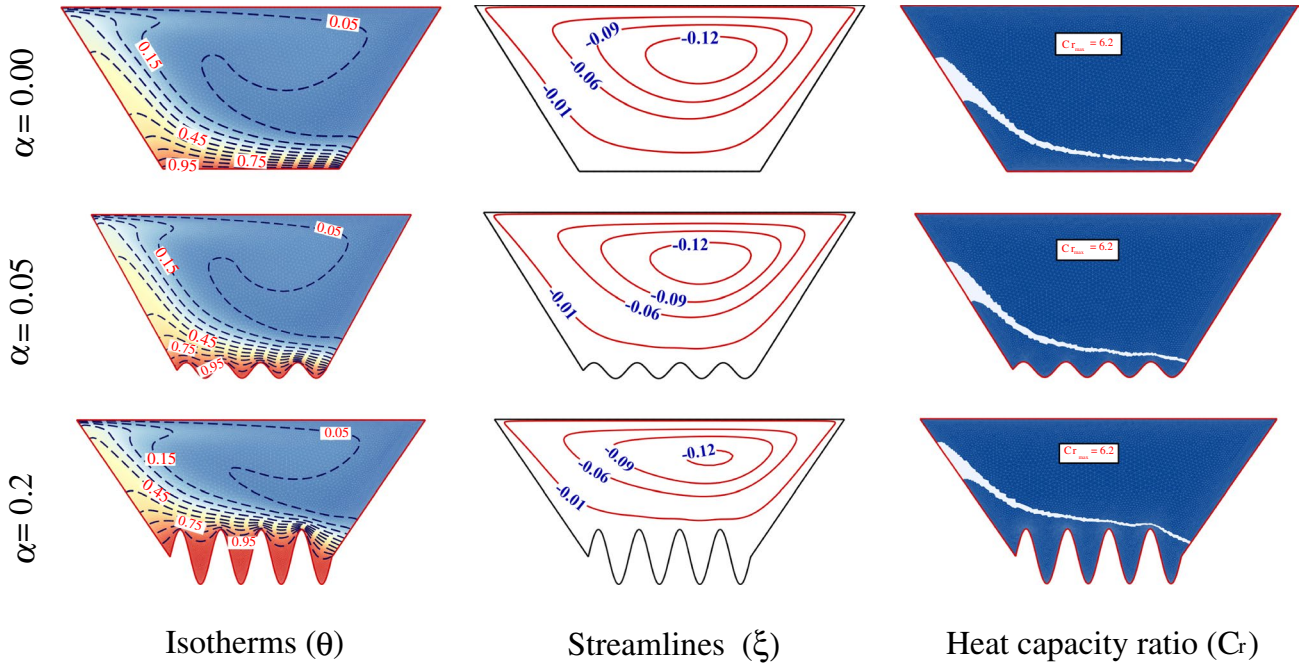

Fig. 8 Field variables for three wave amplitudes of $a=0$, $a=0.05$, and $a=0.2$

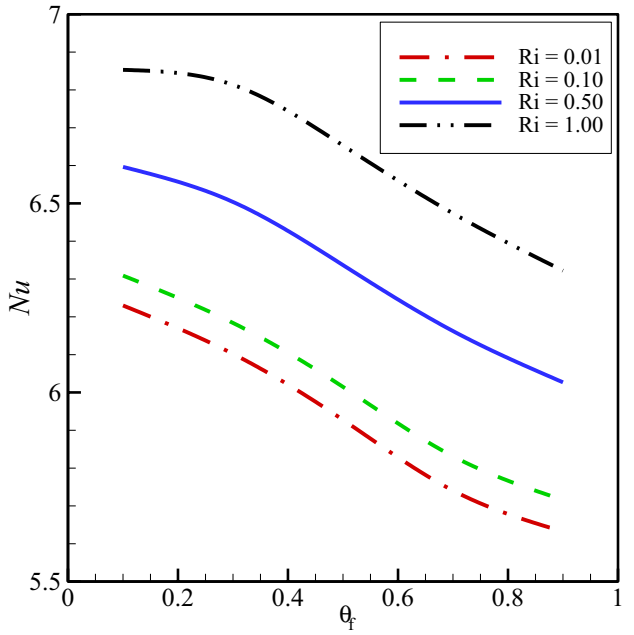

Fig. 9 Influence of fusion temperature (θ_f) and Richardson number (Ri) on *Nu*

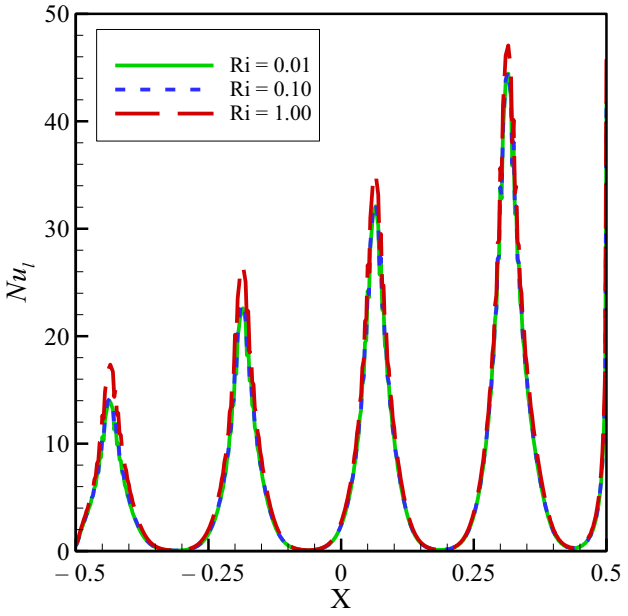

Fig. 10 Local Nusselt number for three Richardson numbers (Ri): Ri = 0.01, Ri = 0.10, and Ri = 1.0

particle fraction $\varphi=0$, the base fluid achieves a Nusselt number of only 5.7. Therefore, it can be concluded that incorporating NEPCM particles leads to a remarkable improvement in heat transfer performance. Specifically, a 37% enhancement in the overall heat transfer is achieved due to the presence of these particles. This observation underscores the significant role that NEPCM particles can play in optimizing heat transfer processes.

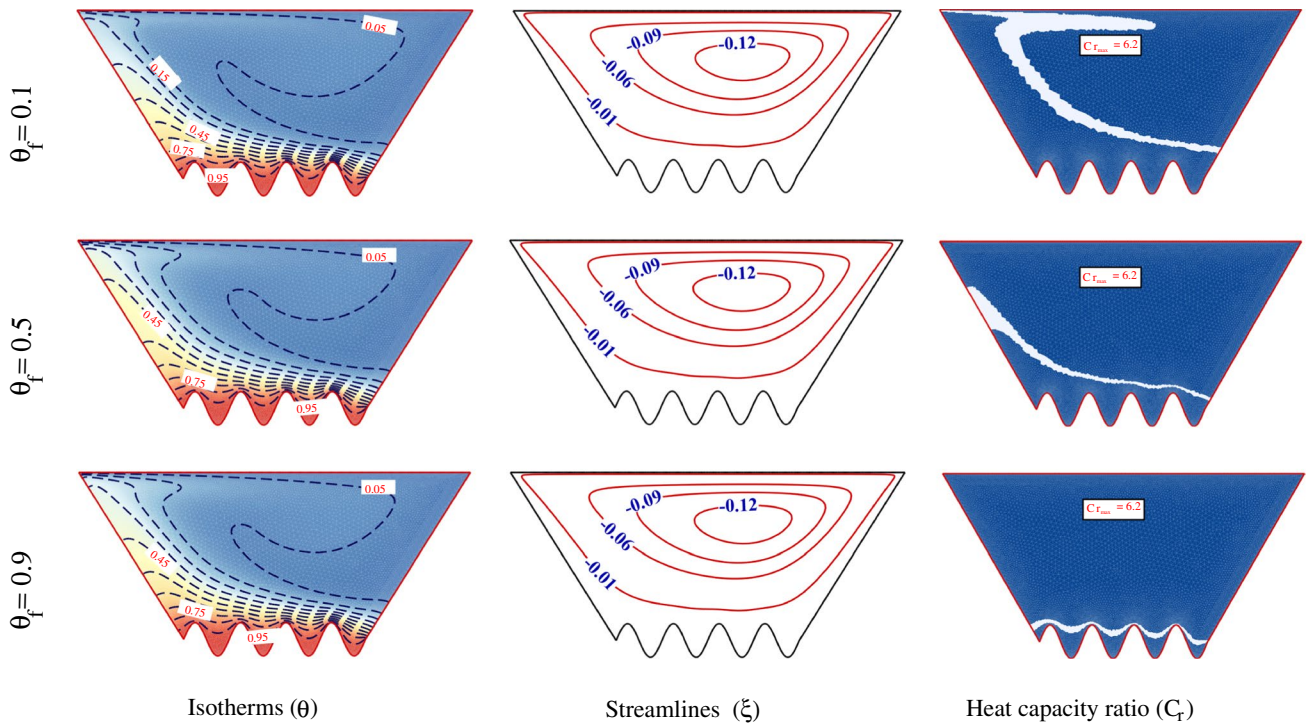

Fig. 11 Field variables for three fusion temperatures $\theta_f = 0.1$, $\theta_f = 0.5$, and $\theta_f = 0.9$

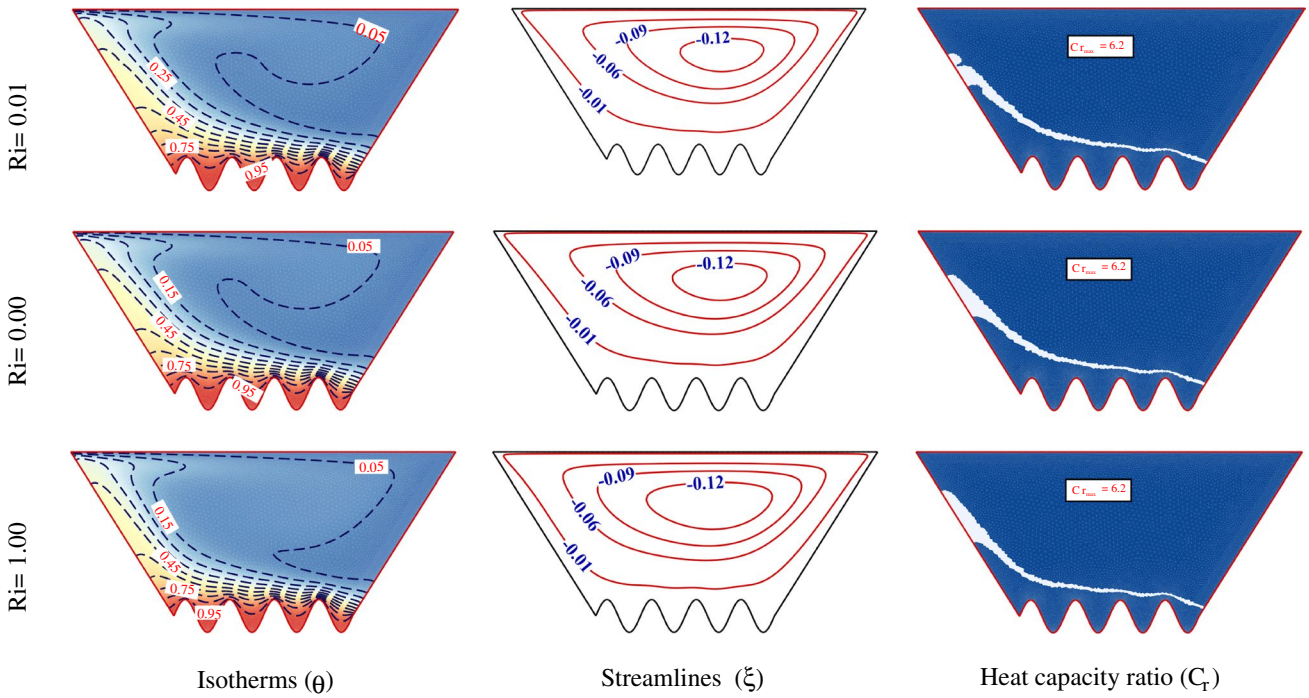

Fig. 12 Field variables for three Richardson numbers Ri = 0.01, Ri = 0.10, and Ri = 1.0

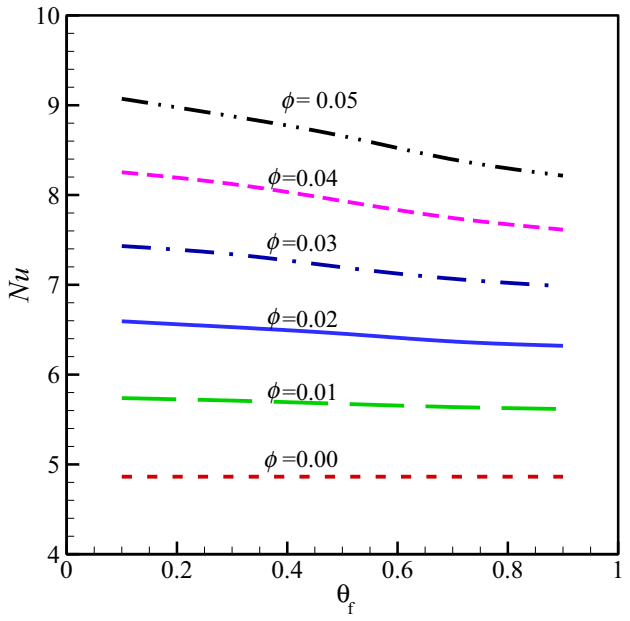

Fig. 13 Impact of nanoparticles fusion temperature (θ_f) and concentration (ϕ) on *Nu*

Conclusions

This study delves into the mixed convection characteristics of NEPCM suspensions in a uniquely configured trapezoidal cavity driven by a lid and exhibiting a wavy base that serves as a hot bottom wall. The nanoparticles suspended in the water-based mixture signify a distinct volume ratio and demonstrate phase transition capabilities, alternating between solid and liquid states as they traverse the enclosure. This transformation allows them to absorb or discharge latent heat at a specific fusion temperature and better contribute to heat transfer. A finite element methodological approach was utilized to integrate the governing equations for heat transfer. The findings are systematically presented through a series of Nusselt number graphs for comprehensive heat transfer evaluation and intricate contour maps of field variables, expanding the current physical knowledge of the underlying heat transfer phenomenon. The main findings of the study include:

1. Examination of the impact of wave amplitude (a) and wavelength (ω) on the average Nusselt number demonstrates a positive correlation, with both parameters enhancing heat transfer efficiency. An increase in wave amplitude (a) results in sharp spikes in the local Nusselt number at each wave's peak, contrasted by a sharp decrease within each wave's trough.
2. The influence of Richardson number and fusion temperature on Nu is also significant. Specifically, an increase in Ri contributes to an elevation of Nu, while a rise in fusion temperature reduces Nu. A rise in Ri promotes stronger natural convection circulation, improving temperature gradients along the wavy wall, particularly at peaks. An 8% enhancement in heat transfer rate can be achieved by merely adjusting the fusion temperature of the NEPCM particles.
3. Increasing the fraction of NEPCM particles in the suspension enhances the Nusselt number, contributing positively to heat transfer efficiency. This effect is attributed to the increased thermal conductivity and heat capacity ratio of the suspension. A peak heat transfer performance can be achieved when the fusion temperature aligns closely with the temperature of the top lid-driven wall. For instance, a configuration utilizing 5% NEPCM particles at a fusion temperature of $\theta_f = 0.1$ results in a Nusselt number of 9.05, a remarkable 37% enhancement compared to the base fluid with a particle fraction of $\varphi = 0$ ($Nu = 5.7$).

Author contributions MG performed conceptualization, methodology, software, validation, formal analysis, data curation, and supervision. KAA provided visualization, original draft preparation, investigation, formal analysis, and data curation. MM did visualization, original draft preparation, investigation, formal analysis, and data curation. TY carried out investigation, writing—review & editing, and supervision. MSI presented visualization, original draft preparation, investigation, formal analysis, and data Curation. NAS developed methodology, software, formal analysis, and data curation. MB conducted methodology, formal analysis, data curation, investigation, and writing—review & editing.

References

1. Ghoghaei MS, Mahmoudian A, Mohammadi O, Shafii MB, Jafari Mosleh H, Zandieh M, et al. A review on the applications of micro-/nano-encapsulated phase change material slurry in heat transfer and thermal storage systems. J Therm Anal Calorim. 2021;145:245–68.
2. Liu C, Rao Z, Zhao J, Huo Y, Li Y. Review on nanoencapsulated phase change materials: preparation, characterization and heat transfer enhancement. Nano Energy. 2015;13:814–26.
3. Ho C, Liu Y-C, Ghalambaz M, Yan W-M. Forced convection heat transfer of Nano-encapsulated phase change material (NEPCM) suspension in a mini-channel heatsink. Int J Heat Mass Transf. 2020;155: 119858.
4. Albdour SA, Haddad Z, Sharaf OZ, Alazzam A, Abu-Nada E. Micro/nano-encapsulated phase-change materials (ePCMs) for solar photothermal absorption and storage: fundamentals, recent advances, and future directions. Prog Energy Combust Sci. 2022;93: 101037.
5. Alehosseini E, Jafari SM. Micro/nano-encapsulated phase change materials (PCMs) as emerging materials for the food industry. Trends Food Sci Technol. 2019;91:116–28.
6. Yang L, Du K. A comprehensive review on the natural, forced, and mixed convection of non-Newtonian fluids (nanofluids) inside different cavities. J Therm Anal Calorim. 2020;140:2033–54.

7. Mustafa MAS, Hussain HM, Abtan AA, Habeeb LJ. Review on mixed convective heat transfer in different geometries of cavity with lid driven. J Mech Eng Res Dev. 2020;43(7):12–25.
8. Alshuraiaan B, Pop I. Numerical simulation of mixed convection in a lid-driven trapezoidal cavity with flexible bottom wall and filled with a hybrid nanofluid. Eur Phys J Plus. 2021;136(5):1–18.
9. Ishak MS, Alsabery AI, Hashim I, Chamkha AJ. Entropy production and mixed convection within trapezoidal cavity having nanofluids and localised solid cylinder. Sci Rep. 2021;11(1):14700.
10. Qasem NA, Abderrahmane A, Khetib Y, Rawa M, Abdulkadhim A, Eldin SM, et al. Mixed convection within trapezoidal-wavy enclosure filled with nano-encapsulated phase change material: effect of magnetohydrodynamics and wall waviness. Case Stud Therm Eng. 2023;42: 102726.
11. Shankar P, Deshpande M. Fluid mechanics in the driven cavity. Annu Rev Fluid Mech. 2000;32(1):93–136.
12. Ece MC, Büyük E. Natural-convection flow under a magnetic field in an inclined rectangular enclosure heated and cooled on adjacent walls. Fluid Dyn Res. 2006;38(8):564.
13. Ahmed SE, Alhazmi M. Impacts of the rotation and various thermal conditions of cylinders within lid-driven enclosures filled with glass balls in the presence of radiation: FEM simulation. Int Commun Heat Mass Transf. 2021;128: 105603.
14. Keya S, Yeasmin S, Rahman M, Karim M, Amin M. Mixed convection heat transfer in a lid-driven enclosure with a double-pipe heat exchanger. Int J Thermofluids. 2022;13: 100131.
15. Mahmud MJ, Rais AI, Hossain MR, Saha S. Conjugate mixed convection heat transfer with internal heat generation in a lid-driven enclosure with spinning solid cylinder. Heliyon. 2022;8(12).
16. Mansour M, Ahmed SE, Aly AM, Raizah ZA, Morsy Z. Triple convective flow of micropolar nanofluids in double lid-driven enclosures partially filled with LTNE porous layer under effects of an inclined magnetic field. Chin J Phys. 2020;68:387–405.
17. Mondal P, Mahapatra T. MHD double-diffusive mixed convection and entropy generation of nanofluid in a trapezoidal cavity. Int J Mech Sci. 2021;208: 106665.
18. Alsabery AI, Ismael MA, Chamkha AJ, Hashim I. Impact of finite wavy wall thickness on entropy generation and natural convection of nanofluid in cavity partially filled with non-Darcy porous layer. Neural Comput Appl. 2020;32(17):13679–99.
19. Golab E, Goudarzi S, Kazemi-Varnamkhasti H, Amigh H, Ghaemi F, Baleanu D, et al. Investigation of the effect of adding nano-encapsulated phase change material to water in natural convection inside a rectangular cavity. J Energy Storage. 2021;40: 102699.
20. Zidan A, Nayak M, Karimi N, Dogonchi AS, Chamkha AJ, Hamida MBB, et al. Thermal management and natural convection flow of nano encapsulated phase change material (NEPCM)-water suspension in a reverse T-shaped porous cavity enshrining two hot corrugated baffles: a boost to renewable energy storage. J Build Eng. 2022;53: 104550.
21. Hussain S, Alsedias N, Aly AM. Natural convection of a water-based suspension containing nano-encapsulated phase change material in a porous grooved cavity. J Energy Storage. 2022;51: 104589.
22. Aly AM, Mohamed EM, El-Amin MF, Alsedais N. Double-diffusive convection between two different phases in a porous infinite-shaped enclosure suspended by nano encapsulated phase change materials. Case Stud Therm Eng. 2021;26: 101016.
23. Aly AM, Raizah Z, El-Sapa S, Oztop HF, Abu-Hamdeh N. Thermal diffusion upon magnetic field convection of nano-enhanced phase change materials in a permeable wavy cavity with crescent-shaped partitions. Case Stud Thermal Eng. 2022;31: 101855.
24. Herouz K, Laidoudi H, Aissa A, Mourad A, Guedri K, Oreijah M, et al. Analysis of nano-encapsulated phase change material confined in a double lid-driven hexagonal porous chamber with an obstacle under magnetic field. J Energy Storage. 2023;61: 106736.
25. Sadr AN, Shekaramiz M, Zarinfar M, Esmaily A, Khoshtarash H, Toghraie D. Simulation of mixed-convection of water and nano-encapsulated phase change material inside a square cavity with a rotating hot cylinder. J Energy Storage. 2022;47: 103606.
26. Mehryan S, Raahemifar K, Gargari LS, Hajjar A, El Kadri M, Younis O, et al. Latent heat phase change heat transfer of a nanoliquid with nano–encapsulated phase change materials in a wavy-wall enclosure with an active rotating cylinder. Sustainability. 2021;13(5):2590.
27. Barlak S, Sara ON, Karaipekli A, Yapıcı S. Thermal conductivity and viscosity of nanofluids having nanoencapsulated phase change material. Nanoscale Microscale Thermophys Eng. 2016;20(2):85–96.
28. Ghalambaz M, Chamkha AJ, Wen D. Natural convective flow and heat transfer of nano-encapsulated phase change materials (NEPCMs) in a cavity. Int J Heat Mass Transf. 2019;138:738–49.
29. Raizah Z, Aly AM. A rotating superellipse inside a hexagonalshaped cavity suspended by nano-encapsulated phase change materials based on the ISPH method. Int J Numer Meth Heat Fluid Flow. 2022;32(3):956–77.
30. Chai L, Shaukat R, Wang L, Wang HS. A review on heat transfer and hydrodynamic characteristics of nano/microencapsulated phase change slurry (N/MPCS) in mini/microchannel heat sinks. Appl Therm Eng. 2018;135:334–49.
31. Chen B, Wang X, Zeng R, Zhang Y, Wang X, Niu J, et al. An experimental study of convective heat transfer with microencapsulated phase change material suspension: laminar flow in a circular tube under constant heat flux. Exp Therm Fluid Sci. 2008;32(8):1638–46.
32. Khanafer K, Vafai K. A critical synthesis of thermophysical characteristics of nanofluids. Int J Heat Mass Transf. 2011;54(19–20):4410–28.
33. Seyf HR, Zhou Z, Ma H, Zhang Y. Three dimensional numerical study of heat-transfer enhancement by nano-encapsulated phase change material slurry in microtube heat sinks with tangential impingement. Int J Heat Mass Transf. 2013;56(1–2):561–73.
34. Zaraki A, Ghalambaz M, Chamkha AJ, Ghalambaz M, De Rossi D. Theoretical analysis of natural convection boundary layer heat and mass transfer of nanofluids: effects of size, shape and type of nanoparticles, type of base fluid and working temperature. Adv Powder Technol. 2015;26(3):935–46.
35. Chamkha A, Doostanidezfuli A, Izadpanahi E, Ghalambaz M. Phase-change heat transfer of single/hybrid nanoparticles-enhanced phase-change materials over a heated horizontal cylinder confined in a square cavity. Adv Powder Technol. 2017;28(2):385–97.
36. Sakhir Abed AA. Numerical simulation of laminar incompressible driven cavity flow in a l-shape domain. Int J Mech Eng Technol. 2019;10(1):119–32. https://doi.org/10.34218/IJMET.10.1.2019.012.
37. Roy M, Roy S, Basak T. Role of various moving walls on energy transfer rates via heat flow visualization during mixed convection in square cavities. Energy. 2015;82:1–22.
38. Zienkiewicz OC, Taylor RL, Nithiarasu P. The Finite Element Method for Fluid Dynamics. 7th Edition ed. Oxford: Butterworth-Heinemann; 2014.
39. Pepper D. The intermediate finite element method: fluid flow and heat transfer applications. Routledge; 2017.
40. Bollhöfer M, Schenk O, Janalik R, Hamm S, Gullapalli K. State-of-the-art sparse direct solvers. Parallel algorithms in computational science and engineering. 2020:3–33.
41. Bollhöfer M, Eftekhari A, Scheidegger S, Schenk O. Large-scale sparse inverse covariance matrix estimation. SIAM J Sci Comput. 2019;41(1):A380–401.

42. Matin MH, Pop I. Natural convection flow and heat transfer in an eccentric annulus filled by Copper nanofluid. Int J Heat Mass Transf. 2013;61:353–64.
43. Turan O, Sachdeva A, Chakraborty N, Poole RJ. Laminar natural convection of power-law fluids in a square enclosure with differentially heated side walls subjected to constant temperatures. J Nonnewton Fluid Mech. 2011;166(17):1049–63. https://doi.org/10.1016/j.jnnfm.2011.06.003.
44. Moallemi M, Jang K. Prandtl number effects on laminar mixed convection heat transfer in a lid-driven cavity. Int J Heat Mass Transf. 1992;35(8):1881–92.
45. Waheed M. Mixed convective heat transfer in rectangular enclosures driven by a continuously moving horizontal plate. Int J Heat Mass Transf. 2009;52(21–22):5055–63.
46. Iwatsu R, Hyun JM, Kuwahara K. Mixed convection in a driven cavity with a stable vertical temperature gradient. Int J Heat Mass Transf. 1993;36(6):1601–8.